Cement and Concrete Research 38 (2008) 1447–1456

Contents lists available at ScienceDirect

Cement and Concrete Research

journal homepage: http://ees.elsevier.com/CEMCON/default.asp

The nano-mechanical signature of Ultra High Performance Concrete by statistical nanoindentation techniques

Luca Sorelli [a,c,*], Georgios Constantinides [a,b], Franz-Josef Ulm [a], François Toutlemonde [c]

[a] Department of Civil and Environmental Engineering, Massachusetts Institute of Technology, 77 Massachusetts ave, 02139 Cambridge, United States
[b] Department of Mechanical Engineering and Materials Science and Engineering, Cyprus University of Technology, Lemesos, Cyprus
[c] Division for Structures Behavior and Durability (FDOA), University Paris-Est — LCPC (Laboratoire Central des Ponts et Chaussées), 58 Bd Lefebvre, 75732 Paris Cedex 15, France

ARTICLE INFO

Article history:
Received 26 May 2008
Accepted 9 September 2008

Keywords:
Microstructure
Nanoindentation
Micromechanics
High perfomance concrete
Fiber reinforcement

ABSTRACT

Advances in engineering the microstructure of cementitious composites have led to the development of fiber reinforced Ultra High Performance Concretes (UHPC). The scope of this paper is twofold, first to characterize the nano-mechanical properties of the phases governing the UHPC microstructure by means of a novel statistical nanoindentation technique; then to upscale those nanoscale properties, by means of continuum micromechanics, to the macroscopic scale of engineering applications. In particular, a combined investigation of nanoindentation, scanning electron microscope (SEM) and X-ray Diffraction (XRD) indicates that the fiber-matrix transition zone is relatively defect free. On this basis, a four-level multiscale model with defect free interfaces allows to accurately determine the composite stiffness from the measured nano-mechanical properties. Besides evidencing the dominant role of high density calcium silicate hydrates and the stiffening effect of residual clinker, the suggested model may become a useful tool for further optimizing cement-based engineered composites.

1. Introduction

Over the last 15 years Ultra High Performance Concretes (UHPC) have become a vanguard product in industrial and structural applications [5–9] thanks to outstanding properties, such as compressive strength of 150–200 MPa, tensile strength of 8–15 MPa with significant remaining post-cracking bearing capacity, and remarkable fracture energy of 20–30 kJ/m^2 [1,2]. Commercial examples include Reactive Powder Concrete now integrated in the ®Ductal range [1,2], ®BSI Ceracem [3], engineered and ultra-high strength and hybrid fiber-reinforced cement composites [4], etc. The superior performance of these products has been achieved by tailoring their microstructures, that is by maximizing the packing density with very fine minerals, quartz powder and silica fume, and by enhancing the matrix toughness with an optimal fiber reinforcement. Nevertheless, the current knowledge of UHPC microstructure is still limited and mainly stems from image analyses [10–12], which is rather qualitative than quantitative, experimental characterization of transfer properties [13], and X-ray diffraction (XRD) and thermo-gravimetric analysis (TGA) [14]. While the mechanical material improvement has been experimentally verified at the macroscopic scale (see Ref. [15] for ®Ductal FM), the underlying mechanisms at the microscale that deliver this superior response are still not well understood. In this work, we first apply a recently developed statistical nanoindentation technique (SNT) to an UHPC material in order to *quantitatively* characterize the UHPC microstructure [16,17]. This method has been developed to extend the domain of application of classical nanoindentation from monolithic materials to multi-phase composites [18,19]. Previously, classical nanoindentation techniques have been employed to study the local mechanical behavior of cement-based materials, such as the micro-mechanisms of creep in C–S–H phases [20] or the interface transition zone in normal concretes reinforced by an optimal system of polymeric fibers [21]. In contrast, based on a large population of indentation tests, the SNT allows the *in situ* assessment of mechanical properties, volume proportions, packing density distributions of microstructural constituents, as well as the mapping of the microstructural morphology. The application of this technique to cement-based materials led to the identification of the intrinsic properties of two characteristic morphological arrangements of Calcium Silicate Hydrates (C–S–H) in cement based materials, namely the High Density C–S–H (HD C–S–H) and the Low Density C–S–H (LD C–S–H) [22]. These properties were found to be independent of mix proportions and can be considered as intrinsic material properties of cement-based materials [23,24]. Notably, these invariant properties are quite unaffected up to a thermal treatment of 200 °C when dehydration processes take place [24,25]. The SNT has been also applied to study the anisotropic microstructure of bones and shales [18].

With tests carried out on ®Ductal G2FM [26], this paper focuses on the nano-mechanical signature of a wide class of UHPC materials and

* Corresponding author. Division for Structures Behavior and Durability (FDOA), University Paris-Est — LCPC (Laboratoire Central des Ponts et Chaussées), 58 Bd Lefebvre, 75732 Paris Cedex 15, France.
E-mail address: luca.sorelli@lcpc.fr (L. Sorelli).

0008-8846/$ – see front matter © 2008 Elsevier Ltd. All rights reserved.
doi:10.1016/j.cemconres.2008.09.002

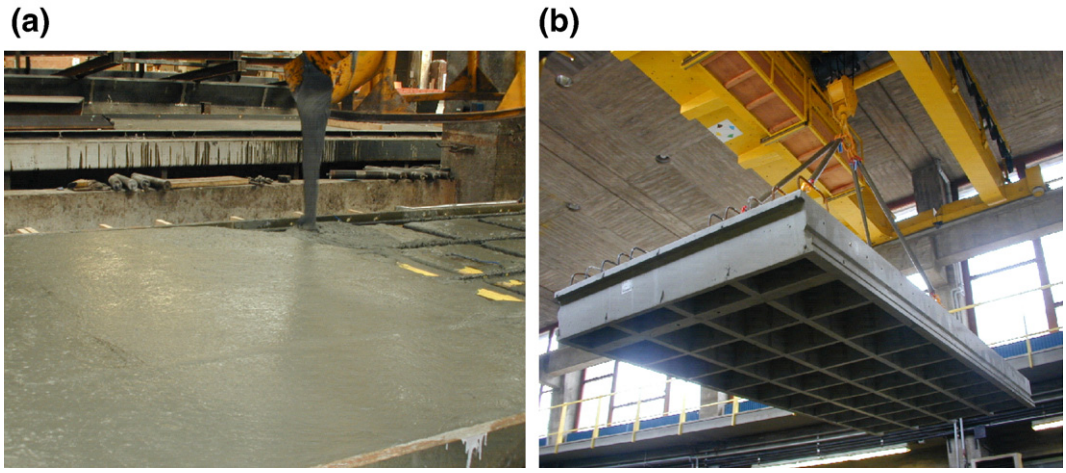

Fig. 1. (a) UHPC casting of the deck model in industrial conditions; (b) the completed deck segment.

on the role of the fiber–matrix interfaces in the homogenized properties. The paper is structured as follows: Following a brief introduction to the SNT method, we present results of an investigation of 'real' UHPC samples which were extracted from reference specimens cast in industrial conditions during the fabrication of a UHPC bridge deck [27]. The fiber–matrix interface zone is studied by line nanoindentation, scanning electron microscope (SEM) and X-ray diffraction analysis (XDR). The experimental results of this work are synthesized into a four-level micromechanics model that aims at linking microstructure and nano-mechanical properties to the macroscopic mechanical performance of UHPC materials.

2. Materials and methods

2.1. Material and sample preparation

To validate design concepts with innovative UHPCs, two 2-way ribbed UHPC deck slab segments (Fig. 1), of dimensions 6.1 m×2.5 m×0.38 m, were cast in industrial conditions within the French MIKTI national R&D project [27]. Six beam specimens for bending tests were cast in the same conditions from the same batch (Fig. 2a), as described in the AFGC Recommendations [8]. A wide experimental campaign with static and dynamic tests was carried out on the bridge segment structure at LCPC Structures Laboratory and details can be found in [28]. For the nanoindentation tests, cylinders with a diameter of 20 mm were cored out from the 50 mm thick beams, and then sliced in penny-shaped specimens of 50 mm-thick (see Fig. 2b). At the time of the nanoindentation tests, the beam specimens had been kept in the 20 to 25 °C, 35 to 55% RH laboratory conditions for about 36 months. The material, which is commercially available by Lafarge, France, under the trade name ®Ductal G2FM [26], was prepared at a water-to-cement ratio w/c between 0.19 and 0.21 using cement CEM I (chemical composition in Table 1), high-range water reducer, silica fume, quartz powder, silica sand and about 2.15% in volume of steel fibers. Compounds dimensions and densities are summarized in Table 2. Silica fume is a by-product of the ferrosilicon alloy industries and has excellent pozzolanic properties. The steel fiber is the largest constituent with a diameter of 0.2 mm and a length of 12.7 mm, while the quartz sand is the largest granular material in the matrix with a diameter varying between 150 and 600 μm (Table 2). In turn, the clinker and crushed quartz are the next to largest particle with an average diameter on the order of 10 μm.

At the 6th day after casting, the material was heat treated to improve strength and dimensional stability by applying, for 48 h, a temperature of 90 °C at a relative humidity of 90%.

The cored cylindrical specimens were sliced into samples of 5 mm thickness. The surface was polished with silicon carbide papers and diamond particles for 8 h according to a standard procedure which

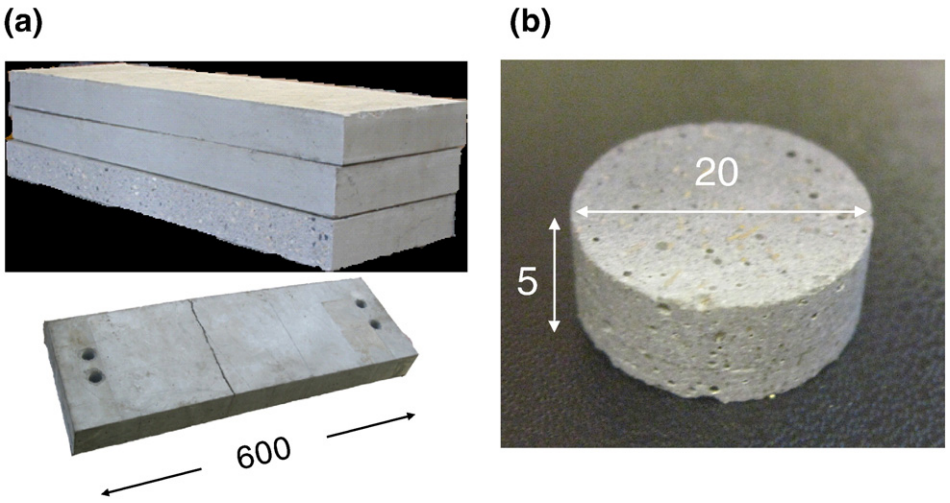

Fig. 2. (a) UHPC plates, 50×200×600 mm, from which samples were cored from; (b) photograph of one of the tested penny-shaped samples.

Table 1
Composition of the cement in mass percentage of each component, as provided by the manufacturer

CaO	SiO_2	Al_2O_3	Fe_2O_3	SO_3	LOI	
67.17	22.14	3.12	2.51	2.13	1.68	
Alite	Belite	Ferrite	Aluminate	Anhydrite	Gypsum	Calcite
71.1	15.0	7.0	1.2	1.4	1.2	1.8

guarantees a root-mean-square roughness inferior to one order of magnitude of the average penetration depth [29].

2.2. SEM and XRD

For SEM and XRD investigation, the surface of the previously indented specimens was metal-coated with carbon (Fig. 2b). High resolution surface inspections of samples were carried out using a Philips XL30 equipped with a microsonde Edax Dx 4i semi-quantitative elemental analysis of solids using energy dispersive X-ray microanalysis at the laboratories of *Physico-Chimie des Matériaux Département*, LCPC. The image analysis is based on measurement of signals resulting from the electron beam-specimen interaction which include secondary electrons (SE) for imaging surface topology; backscattered electrons (BE) for highlighting compositional differences; and X-rays for determining the chemical composition (XRD). Images from an SEM are monochrome since they reflect the electron or X-ray flux resulting from the beam-specimen interaction.

2.3. Nanoindentation investigation

We briefly recall that a nanoindentation test consists of establishing contact between an indenter (typically diamond) and a sample, and subsequently measuring the load, P, and the penetration depth, h (for a comprehensive review see [19]). Fig. 3a shows a typical P–h curve for a test with an initial constantly increasing load, followed by a short hold and then a constant unloading. The analysis of the P–h curve proceeds by applying continuum scale models [30,31] to derive the indentation hardness H and indentation modulus M:

$$H \overset{\text{def}}{=} \frac{P_{\max}}{A_C}, \tag{1}$$

$$M \overset{\text{def}}{=} \frac{\sqrt{\pi}}{2}\frac{S}{\sqrt{A_C}}, \tag{2}$$

All the quantities required to determine H and M are directly obtained from the P–h curves, with exception of the projected area A_c (Fig. 3b). Chief among these are the unloading indentation stiffness $S = (\mathrm{d}P/\mathrm{d}h)_{h=h_{\max}}$, and the residual indentation depth h_f of the material surface after complete unloading (Fig. 3a). The contact area A_C can be extrapolated from the maximum depth $h_{\max}$ using the Oliver and Pharr method [32]. For homogeneous material systems, the indentation modulus M can be linked to the elastic constants of the indented material by applying a linear elastic model to the data [30,31]. In the isotropic case, M reduces to the plane-stress elastic modulus:

$$M = \frac{E}{(1-\nu^2)}, \tag{3}$$

where, E is the Young's modulus and ν is the Poisson's ratio of the indented material. Similarly, the hardness H can be related to strength properties, namely cohesion c and friction angle φ and the cone angle θ by:

$$H \equiv c\Im(\vartheta,\varphi) \tag{4}$$

where $\Im(\vartheta,\varphi)$ is a dimensionless function that can be determined from advanced yield design solutions of the nanoindentation test [33–35].

Fig. 4 shows typical indentation curves for the different mechanical phases identified by the deconvolution analysis presented hereafter. Irregular or discontinuous indentation curves may occur due to cracking phenomena and can not be considered by the underlying contact model [30,31].

Recognizing the highly heterogeneous nature of cement-based materials in general and UHPC in particular, a large array of nano-indentation tests needs to be carried out and analyzed statistically. The premise of this statistical nanoindentation technique (SNT) is that each indentation test is a single statistical event and that the properties extracted from continuum indentation analysis are random variables (Fig. 5). Typically, a large series of indentation tests are carried out on a grid of the surface sample; for instance, 100 indentations are sufficient to guarantee a convergence on the elastic property of *LD* and *HD C–S–H* with an error inferior than 5% [36]. The data are then analyzed by *deconvoluting* the discrete experimental distribution values $P(x)$ of the mechanical properties $x=(H, M)$ by the sum of n theoretical probability distribution functions p_J, one for each mechanically distinct phase [16,18]:

$$\min P(x) = \sum_{i=1}^{m}\sum_{x=(M,H)}\left(\sum_{j=1}^{n} f_J p_j\left(x_i,\mu_J,s_J\right) - P(x_i)\right)^2 \; s.t. \quad \sum_{J=1}^{n} f_J = 1 \tag{5}$$

where μ_J and s_J are the mean and standard deviation of $x=(M, H)$ of the phase $J=1, n$; f_J is the volume fraction of the phase composing the heterogeneous material; $P(x_i)$ is the measured value of the normalized frequency; m is the number of intervals (bins) by which the problem is discretized; and p_J is the value of the theoretical probability density function of the single phase, which is assumed to be a normal distribution:

$$p_J = \frac{2}{\sqrt{2\pi s_J^2}}\exp\left(\frac{-\left(x-\mu_J\right)2}{2s_J^2}\right), \tag{6}$$

where μ_J and $s_J(H)$ stand for mean and standard deviation, respectively. The minimization of Eq. (5) is done simultaneously for the frequency distributions of the indentation modulus M and the hardness H. The results of the deconvolution technique are the mean and standard deviation of the indentation modulus and hardness, and the volume fraction for each phase, i.e., $\{\mu_J(x), s_J(x), f_J\}$, of $x=(M, H)$, for $j=1, n$. In addition, to identify statistically relevant phase properties with a sufficient contrast, the overlap of successive Gaussian curves representative of two phases is constrained by:

$$\mu_J^x + s_J^x < \mu_{J+1}^x + s_{J+1}^x \quad x = (M,H). \tag{7}$$

To ensure that indentation results do not depend on any characteristic length, the scale separability condition must be verified for each phase:

$$d/10 \;<<\; h_{\max} \;<<\; D/10, \tag{8}$$

where d and D stand for the characteristic sizes of the largest heterogeneity (particle size) and of the representative element

Table 2
Mean particle size and apparent density of the UHPC compounds

Material	Mean particle size [μm]	specific gravity [kg/m^3]
Cement CEM I	10–25	3150
Silica fume	0.1–1	2220
Quartz powder	0.1–100	2650
Quartz sand	150–600	2650
Steel fibers	200 (diameter)	7850
Superplasticizer	–	1070
Water	–	1000

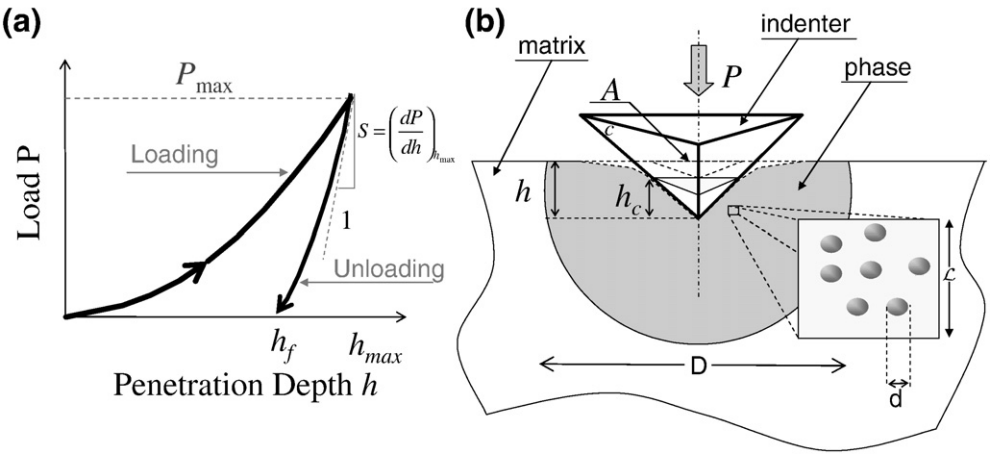

Fig. 3. (a) A typical load-indentation depth *P*–*h* curve; (b) Schematic representation of an indentation test with a Berkovic indenter on a homogeneous phase.

volume, respectively (Fig. 3b). In other words, for $h_{max}<d$ the indentation response will be affected by the heterogeneity dimension of the phase, and for larger depth $h_{max}>D$ the indentation depth will be affected by the interaction of different phases of the microstructure.

The nanoindentation tests were performed at the Nano Mechanical Technology Laboratory in the Department of Materials Science and Engineering, MIT using a commercially available nanoindenter (NanoTest, MicroMaterials Ltd.). The penetration depth h is continuously recorded by the change in the capacitance of a parallel plate capacitor, while the motion of the indenter into the surface is controlled by an electro-magnetic pendulum device pivoting around frictionless bearings. The test setup allows monitoring the *P*–*h* relationship in a load range of 0 to 500 mN, and in a displacement range of 0 to 20 μm, with resolutions of 3 nN and 0.06 nm, respectively [36]. The three-sided pyramidal Berkovich indenter shape constructed with a semi-vertical angle of 65.3° was chosen, since it reduces the pile-up phenomena around the indented area, which are not explicitly accounted for by the adopted model in determining the contact area A_C [32]. During the test calibration, the area function of the indenter was obtained by indenting a calibration material (quartz) of known mechanical properties in the depth range of 5–600 nm. The depth range was chosen to be close to the range of depth used during our experimental investigation on UHPC such as to avoid discrepancies being introduced in the analysis due to any geometric artifacts. The discrete data points were fitted with a polynomial function of the form $Ac=C_0h_c^2+C_1h_c+C_2h_c^{1/2}$ where $C_0=25.98$, $C_1=929.34$, $C_2=-140.47$ [16,36]. The accuracy of the function was further verified using atomic force microscopy images of the indenter tip [37].

A trapezoidal loading history was prescribed, defined by a loading time $\tau_L=10$ s, a holding time $\tau_H=5$ s at $P_{max}=2$ mN, and an unloading time $\tau_U=10$ s. The results during the holding phase can be employed to study the creep behavior of the UHPC constituents at small scale, however they are not presented in this work which focuses on the elastic properties (the portion of the *P*–*h* curve during the holding phase has been not included in Fig. 4). Each single test consists of a line of 100 indentations with a spacing length of $h=5$ μm to better detect possible transition zone, but sufficiently large to avoid any interaction between two adjacent indentations (e.g., $h=10$ μm in [36] and $h=5$–8 μm in [21]). Seven test series were carried out by randomly choosing the position of the line on the sample surface for a total population of 700 indentations.

The *P*–*h* curves were examined in order to determine the validity of each curve. Less than 5% discontinuous displacement plots were observed with a 'jump' in the indentation depth (Fig. 4) which may relate to cracking. Provided that the maximum penetration depth h_{max}, which varies from 50 to 300 nm, satisfies the separability scale condition of Eq. (8), the SNT provides access to the properties of each phase. For instance, prime candidate for d is the size of the single colloidal gel particles of ~5 nm or the size of C–S–H sheet which is less than 2 nm, whereas the characteristic size D of a well hydrated cement paste is on the order of 1–3 μm [22,24]. Analogously, the grain dimension D for the quartz powder, residual clinker, quartz sand is estimated to be, respectively, 0.1 100 μm, 1–10 μm, 150–600 μm, whereas the crystal size of each phase is expected to be much smaller than h_{max}.

3. Results and discussion

3.1. Microstructure images

Fig. 6 shows SEM images at different length scales from 10^{-4}–10^{-5} m. At the scale of 400 μm, it is possible to discern inclusions of fibers and quartz sand within the cement paste. At a smaller scale, several residual clinker particles with a diameter of approximately 10 μm are visible in the cement paste. The powder quartz looks like tiny grains embedded in the paste and, as the sharp edges indicate, they are expected not to have reacted with the surrounding paste. However, recent studies with high resolution SEM have shown that the finest fraction of powder quartz (with size inferior of 1 μm) can react with the pore solution [12]. No portlandite crystals (or calcium hydroxide, CH) and silica fume were observed, and can be considered to have been fully converted into C–S–H by the pozzolanic reaction. The zone surrounding the fibers appears compact, although few microcracks can be detected in the vicinity of the sand particles.

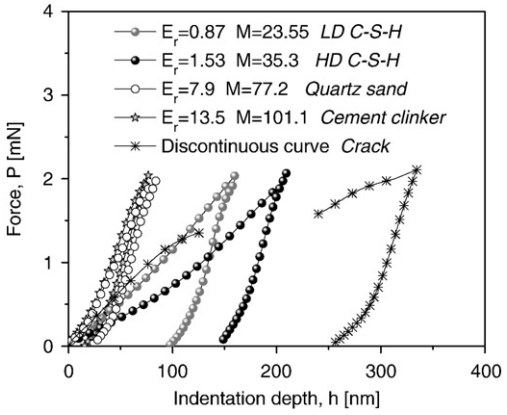

Fig. 4. Indentation response force, P, vs. indentation depth, h.

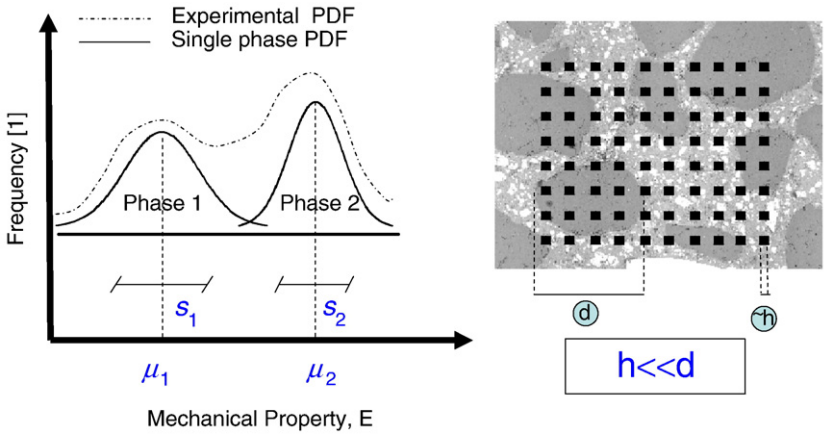

Fig. 5. Schematic representation of the deconvulution techniques for composite materials.

3.2. Deconvolution results

Based on the SEM observations of this study and previous results on cement pastes [22,36], it is reasonable to assume that the hardened UHPC microstructure is composed of, at least, the following $n=8$ phases:

- Phase 1–2) Calcium Silicate Hydrates (C–S–H) organized into, at least, two forms, LD C–S–H and HD C–S–H, which have their own morphological arrangement, packing density and mechanical properties [22,23,36];
- Phase 3) Residual Cement Clinker (CC) is always present in cement-based materials with a water-to-cement ratio $w/c<0.42$; and, as the hydration proceeds, the smallest particles dissolve first, and the large ones gradually start decreasing in size [20,38];
- Phase 4–5) Porosity shows a large range of size distribution and includes capillary Porosity (P) with pore size between 10 nm and 10 μm and the Air Voids (AV) due to improper vibration and/or high fresh UHPC viscosity (disconnected bubbles as large as 3 mm). Note that the intrinsic gel-porosity with a size between 0.2 nm to 10 nm cannot be assessed directly by nanoindentation, but needs to be analyzed from scaling relations [17,36].
- Phase 6) Powder Quartz (PQ) has a particle size distribution ranging from 0.1 to 100 μm and is generally considered as inert, although smallest particles with size of 1 μm may react with the pore solution to form further C–S–H [12];
- Phase 7) Quartz Sand (QS) has a particle size distribution ranging from 150 to 600 μm and is dimensionally the largest granular material and is not reactive;
- Phase 8) The Steel Fibers (SF) are straight steel wires with a nominal diameter of 0.2 mm and a nominal length of 12.7 mm.

By minimizing Eq. (5) for $n=8$ phases, the deconvolution technique provides the mechanical properties of each mechanically distinct phase. The experimental frequency plots (normalized histogram) for indentation modulus (M) and hardness (H) are displayed in Fig. 7a and b, respectively, showing an accurate modeling of the experimental probability distribution function (PDF). For Quartz Powder (QP) and Quartz Sand (QS), the constraint condition (7) was released, since they are mainly made of the same chemical composition, i.e., silica. In return,

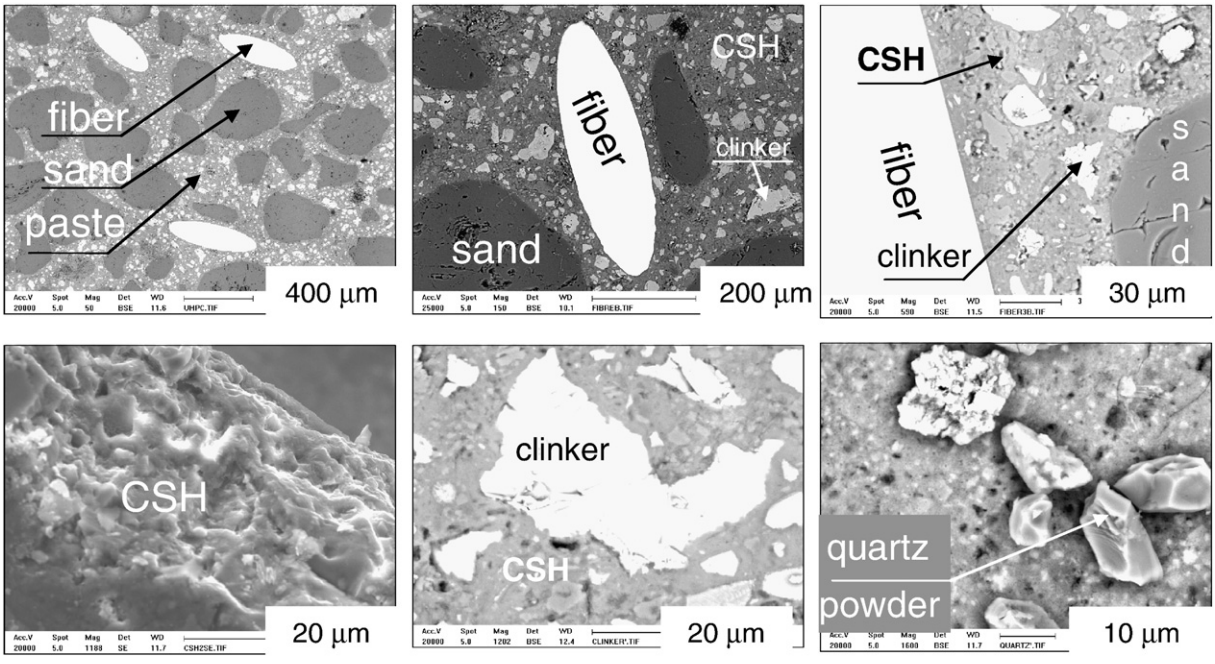

Fig. 6. SEM images of the UHPC microstructure.

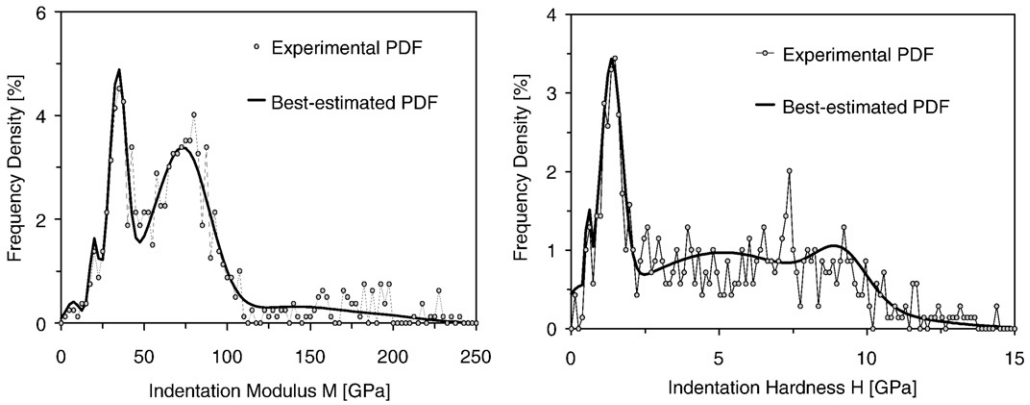

Fig. 7. Experimental frequency plots and the best-estimated PDF evaluated from the deconvolution technique for the indentation modulus *M* (a) and the indentation hardness *H* (b).

for forthcoming developments the difference in their mean particle size requires to consider them as two separate phases. For the deconvolution algorithm, the initial values are derived from typical Powers reaction formula with ®Ductal FM mix-proportions [2,9,20,26]. The deconvolution results are displayed in Fig. 7a and b as best-estimated PDF and in Fig. 8a and b as the PDFs of each microstructure constituent for the indentation modulus (*M*) and hardness (*H*). Table 3 summarizes the results of the deconvolution optimization process in terms of volumetric proportion, the mean and standard deviation of the indentation modulus (*M*) and hardness (*H*) for each phase as well as reference values from the open literature. The *intrinsic* elastic properties summarized in Table 3 differ up to 15%, which is a fairly good agreement considering the experimental measurements' errors arising from material variability (chemical, casting, polishing…) and instrumented calibration.

The mean values of the indentation modulus of the LD and HD C–S–H phases are in good agreement with the characteristic values found for different cement pastes [21,22,24,25,29,36]. The first peak with a mean hardness value of 2.5 MPa in the indentation modulus plot of Figs. 7a and 8a relates to the weakening effect of the microporosity on the C–S–H matrix and can be taken as an indirect measure of the capillary porosity [24,36]. A notable result is that the volume fraction of HD C–S–H is about 86% percent of the overall volume of the C–S–H matrix, which is of course much higher than the value of about 30% which is found for materials with a $w/c = 0.5$ [22,36]. Furthermore, the cement clinker (CC) characterized by a very high modulus 141 ± 34.8 GPa with a large standard deviation, has a volume content of about 11%, which is in line with the theoretical prediction from the hydration reactions [20,38]. The residual cement clinker is expected to stiffen the overall response [20,38–40], while the high scatter may depend on the several clinker compounds (such as calcium silicate, calcium aluminate and calcium aluminoferite) which are not individually discernable by the present technique. Similar results are obtained for the hardness values which are summarized in Table 3, and which show a fairly good agreement with reference values reported in the open literature. Notably the hardness of HD C–S–H is slightly enhanced with respect to the values reported for cement paste samples [36]. The hardness value of the clinker, equal to about 10 GPa, agrees well with previous results on pure clinker phases [20,38], while the high scatter of the hardness values (Fig. 7b) has been normally found in heterogeneous cement pastes [20,36]. Finally, the limited accuracy of the SNT in determining the hardness' values of the quartz phases with respect to the reference values [20] is due to the rather flat frequency between 2.5 and 10 GPa in the corresponding frequency plot (Table 3; Fig. 8b). The inaccuracy in determining the fiber volume content can be imputed to the low volume fiber content and the relative large size of fiber length with respect the analyzed length.

4. Fiber–matrix interface zone

This section focuses on the characterization of the Interface Transition Zone (ITZ) around the fibers, which plays an essential role in the mechanical behavior, fatigue life and durability of conventional fiber reinforced concrete [40,41]. The ITZ was characterized by XRD analysis and nanoindentation along point lines of 60 μm length from the fiber surface with a 5 μm spacing.

4.1. XRD investigation

The chemical composition was measured on 6 lines starting from the fiber surface of different randomly chosen fibers. Fig. 9a displays the mean chemical composition at different distances from the fiber surface. No significant change of chemical composition is revealed. This hints towards a uniform composition of the hydration products in

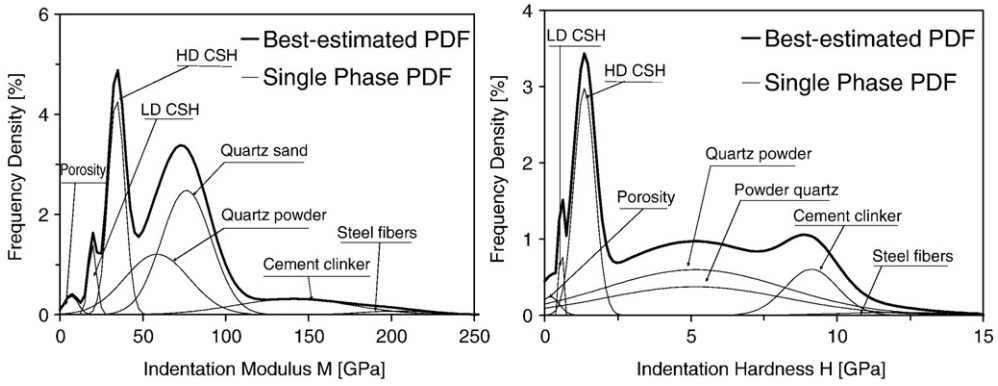

Fig. 8. The overall simulated PDF is the sum of single phase PDF evaluated from the deconvolution technique for the indentation modulus *M* (a) and the indentation hardness *H* (b).

Table 3
Results from the deconvolution analysis with reference values from open literature (references in squared brackets)

Microstructure phase	Extracted values			Reference values	
	Volume fraction	Modulus	Hardness	Modulus	Hardness
	f [%]	*M* [GPa]	*H* [GPa]	*M* [GPa]	*H* [GPa]
Micro porosity	1.5	7.0±4.0	0.19±0.30	9.1±2.3 [36]	0.16±0.07 [36]
LD C–S–H	3.5	19.7±2.5	0.55±0.03	19.1±5.0 [24] 21.7±2.2 [22] 20.2±2.0 [20] 18.8±4.0 [36] 23.7±0.8 [39]	0.80±0.20 [20] 0.66±0.3 [24] 0.47±0.17 [36] 0.93±0.11 [39]
HD C–S–H	21.5	34.2±5.0	1.36±0.35	29.4±2.4 [22] 31.0±4.0 [20] 32.3±3.0 [24] 32.3±2.6 [39]	0.9±0.3 [20] 1.29±0.1 [24] 1.22±0.07 [39]
Quartz powder	23.5	58.5±19.4	5.14±3.08	–	–
Quartz sand	37.5	76.3±15.1	5.14±3.08	73±1.6 [20]	10±0.3[20]
Cement clinker	11.0	141.1±34.8	9.12±0.90	125–145±25 [20,38] 126.8±8.1 [39]	8–10.8±3 [20,38] 6.7±1.2 [39]
Steel fiber	1.5	201.9±20.3	11.99±1.97	–	–

the C–S–H matrix shell of 60 μm thickness surrounding the fiber, at least with a spatial resolution of 5 μm.

4.2. Indentation analysis

Fig. 9b shows the mean value of the indentation stiffness at 12 points adjacent to a fiber surface (within a distance of 60 μm). The scatter and the normal distribution of the indentation modulus at different distances are plotted as well. The stiffness in the zone surrounding the fiber decreases along the radial direction to approach at a distance equal to the fiber radius (~100 μm) the value of the surrounding UHPC matrix. This stiffness gradient may be attributed to a possible fiber influence on the UHPC matrix apparent rigidity. This result clearly indicates that the ITZ around fibers is not softer than the bulk matrix as for ordinary cement composites [41] or for engineering cement composites [21].

5. Discussion: a multi-scale model for UHPC

The combination of nanoindentation, SEM and XRD provides strong evidence that the macroscopic performance of UHPC materials is determined by two factors that occur at different scales: (1) at a nanoscale, the pre-dominance of HD C–S–H among the cement hydration products (Fig. 8a and b); and (2) at a microscale, the absence of a weak transition zone between the fibers and the surrounding cement paste matrix (Fig. 9a and b). These two characteristics distinguish UHPC materials from normal fiber reinforced materials, prepared at higher *w*/*c* ratios, in which the bulk behavior of the cement paste is dominated by LD C–S–H, and in which a weak fiber–matrix interface becomes a limiting factor of the material performance [41]. We thus suggest that those two phenomena are intimately related; that is, the higher density of the C–S–H entails an improved transition zone, which ultimately translates into the Ultra-High Performance of UHPC materials.

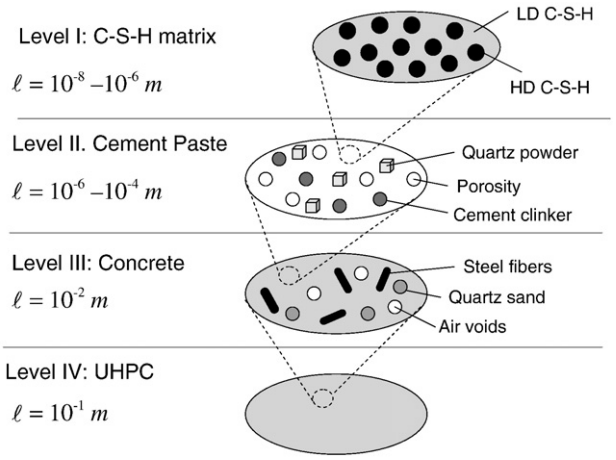

Fig. 10. Four-level scale model for UHPC.

To illustrate our purpose, we consider a four-level multiscale thought model for fiber reinforced cement-based materials as shown in Fig. 10. In this model, we exclude the presence of any weak interfacial zone. A comparison of model predictions with experimental data provides evidence of the relevance of our suggestion.

In this multiscale model, each scale verifies the scale separability condition (8), i.e., each level is separated from the next one by one order of magnitude in size of the elementary heterogeneity. For this model, we determine the macroscopic elasticity by means of linear micromechanics which accounts for inclusion interactions.

To do so, we use the classical tools of linear continuum micromechanics, namely the strain localization relations [42,43]:

$$\varepsilon(\mathbf{x}) = \mathbf{A}(\mathbf{x}) : \mathbf{E} \tag{9}$$

where $\varepsilon(\mathbf{x})$ represents the microscopic strain at point $\mathbf{x}$, which is related by the 4th-order localization tensor $\mathbf{A}(\mathbf{x})$ to the macroscopic

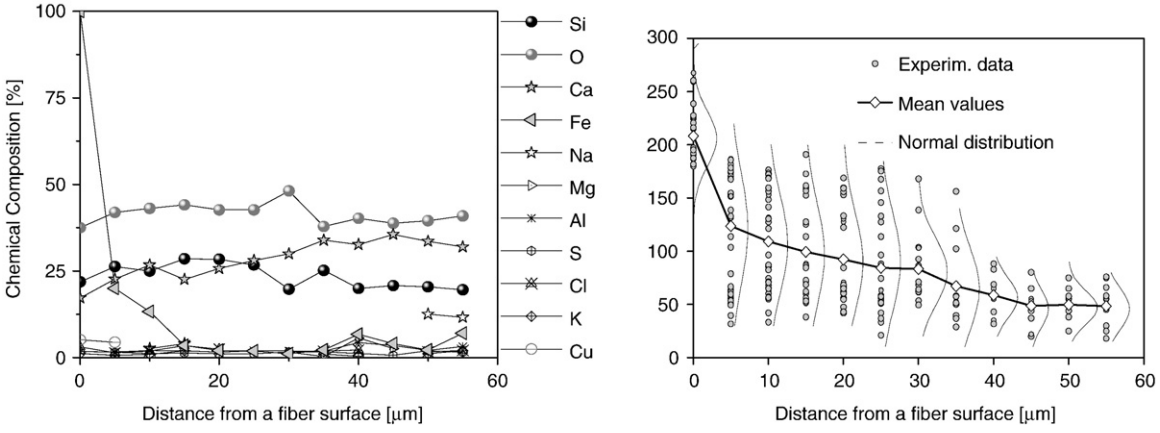

Fig. 9. Chemical composition by X-ray diffraction (a) and indentation modulus *M* (b) along a line of points close to the fiber surface.

Table 4
Input–output of the four-step homogenization model for UHPC

Level I				Level II				Level III			
Input	E [GPa]	ν [l]	f [%]	Input	E [GPa]	ν [1]	f [%]	Input	E [GPa]	ν [1]	f [%]
1. C–S–H–LD	18.6	0.24	14.0	1. C–S–H	29.9	0.24	40.9	1. Paste	58.4	0.21	54.5
2. C–S–H–HD	32.2	0.24	86.0	2. Porosity	0	0	2.4	2. Quartz sand	73.2	0.20	37.5
				3. Powder quartz	48.2	0.20	38.5	3. Fiber	183.7	0.30	1.5
				4. Cement clinker	128.4	0.30	18.0	4. Air voids	0	0	6.5
Output	29.9	0.24		Output	45.3	0.23		Output	48.4	0.22	

strain $\mathbf{E}$. The macroscopic strain $\mathbf{E}$ and the macroscopic stress $\boldsymbol{\Sigma}$ of a representative elementary volume V (REV) are the averages of the microscopic counterparts $\varepsilon(\mathbf{x})$ and $\sigma(\mathbf{x})$:

$$\mathbf{E} = \langle \varepsilon(\mathbf{x}) \rangle_v; \tag{10a}$$

$$\boldsymbol{\Sigma} = \langle \sigma(\mathbf{x}) \rangle_V = \langle \mathbf{C}_r : \varepsilon(\mathbf{x}) \rangle_V \tag{10b}$$

where $\mathbf{C}_r$ is the 4th-order stiffness tensor of the single phase, and $\langle y_v \rangle = 1/V \int y dV$ denotes the volume average of quantity y over domain V. Substituting Eq. (9) and Eq. (10a) into the stress average of Eq. (10b) yields the homogenized stiffness of the composite:

$$\mathbf{C}^{\text{hom}} = \langle \mathbf{C}_r : \mathbf{A}_r \rangle_V = \mathbf{C}_0 + \sum_{r=1}^{n} \langle \mathbf{A}_r \rangle (f_r - f_0) \tag{11}$$

where the subscript "0" stands for the matrix embedding the r inclusion phases. The localization tensor $\mathbf{A}_r$ incorporates information about the morphology of the phase. From a morphological point of view, the four level of Fig. 10 are characterized by a matrix-inclusion geometry that can be effectively treated with the Mori-Tanaka scheme [44]. In this case, the localization tensor estimate of the Mori-Tanaka scheme mathematically reads:

$$\mathbf{A}_r^{\text{est}} = \left[\mathbf{I} + \mathbf{S}_0^{\text{esh}} : \left(\mathbf{C}_0^{-1} : \mathbf{C}_r - \mathbf{I} \right) \right]^{-1} : \left\langle \left[\mathbf{I} + \mathbf{S}_0^{\text{esh}} : \left(\mathbf{C}_0^{-1} : \mathbf{C}_r - \mathbf{I} \right) \right]^{-1} \right\rangle_v^{-1} \tag{12}$$

where $\mathbf{S}_0^{\text{esh}}$ is the Eshelby tensor for a spherical inclusion [43,45]. In the case of randomly oriented fibers, the Eshelby tensor $\mathbf{S}_0^{\text{esh}}$ obtained from a geometric procedure of orientation averaging is still isotropic [43]. This micromechanics scheme is selected for its simplicity and its very good performance in the characteristic range of the multiple phases involved (typically, 0–30%) and for the Poisson's ratios herein considered ($0.2 \le \nu \le 0.3$) [22]. The upscaling scheme of Eq. (11) is applied in three steps according to the multiscale model of Fig. 10. The input–output properties at each homogenization step of the multiscale model are summarized in Table 4 and explained in details in the following.

5.1. Step I: C–S–H matrix

The first homogenization step consists in considering the C–S–H matrix as a two-phase composite: the LD C–S–H plays the role of inclusions embedded in a stiffer HD C–S–H matrix, i.e., "0" = HD C–S–H and r = LD C–S–H in Eq. [11)s. From SNT (Table 3), the volume fraction of the LD C–S–H phase is found to be quite low, and occupies within the C–S–H matrix a volume fraction of $f_{\text{LD C–S–H}} = 3.5/(3.5+21.5) = 14\%$. Since no direct measurements of the Poisson's ratio of C–S–H phases are available, we assumed a Poisson's ratio of 0.24 for both C–S–H phases [22,36]. In any case, its influence on the calculation of the overall elastic modulus is expected to be less than 10% for Poisson's ratio between 0 and 0.5 [17]. The Young's modulus of the two C–S–H phases is then calculated with Eq. (3) from the indentation modulus estimates of Table 3 by assuming (Table 4). The homogenized Young's modulus of the C–S–H matrix is 29.9 GPa, which is significantly higher than that of an ordinary cement paste, i.e., 23.8 GPa for a w/c = 0.5 cement paste [22,36]. This intermediate result shows the key role of the HD C–S–H on the C–S–H matrix properties of a UHPC material. The high volume fraction of HD C–S–H in the cement paste (86% from Table 4) justifies *a posteriori* the choice of the Mori Tanaka's homogenization scheme. We finally remark that a different homogenization scheme such as the self consistent scheme, which is more suitable for granular phases, would yield similar results because of the relatively low volume fraction of LD C–S–H (14%) and the low contrast between the C–S–H phases' properties.

5.2. Step II: cement paste

The second homogenization step, sketched in Fig. 10, consists in bridging from Level I to Level II. In this step, the cement paste is considered as a four phase composite material in which the C–S–H matrix (from the previous step) is a homogenized medium embedding quartz powder (QP), porosity (P) and cement clinker (CC), i.e., "0" = C–S–H matrix, r = {P, CC, QP} in Eq. (11)). The homogenized Young's modulus of the cement paste is 58.4 GPa and the Poisson's ratio is 0.21 (Table 4). The elasticity modulus of the UHPC cement paste is much higher than what is known for normal cement paste materials [36]. This result is a *quantitative* confirmation of previous studies which recognized the stiffening role of the residual clinker on the overall properties of the hardened cement paste [20,38,39].

5.3. Step III: UHPC

The third and final homogenization step considers UHPC as a four-phase composite material, in which the homogenized medium, i.e., the cement paste (CP), forms a matrix that embeds steel fibers (SF), quartz sand (QS), and air voids (AV), i.e., "0" = cement paste from previous step, r = {QS, SF, AV} in Eq. (11).

The volume fraction of air voids cannot be determined from nanoindentation tests, since the scale of disconnected air bubbles, 0.5 to 3 mm-large on average, mainly related to the casting process, exceeds the observation scale and the possibility of a quantitative evaluation by

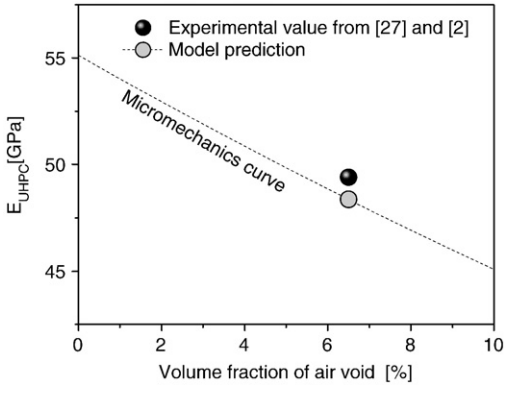

Fig. 11. Sensitivity analysis of the Young's modulus with respect to the air void content.

SNT. From a previous experimental campaign on a similar ®Ductal FM material, the characterization of air void content was carried out on 12 cylindrical specimens of 102 mm diameter with the modified standard method of ASTM C457 [9,46]. For 8 specimens, the filling procedure of the samples was followed by a mechanical vibration for up to 300 s [9]. For each specimen an area of 103 mm^2 was analyzed by counting the voids intercepting a line of 1270 mm. The air void content was estimated to be about 6.5 ± 1.3% with a small effect of the mechanical vibration. As shown in Table 4, the resulting Young's modulus for UHPC is 48.4 GPa. This predicted value is in excellent agreement with the experimental value, 49.4 ± 1.6 GPa measured from the bending tests on the thin beams from which the nanoindentation specimens were cored out [27], or with the value 52.7 ± 1.0 GPa from compression tests on ®Ductal FM cylinders with diameter 76 mm measured according to ASTM C469 [9,47]. A sensitivity analysis has been conducted in order to relate the air void content and the global Young's modulus, as determined by this last-step homogenization (Fig. 11). The relationship between the elastic modulus and the air void content up to 10% is approximately linear. The order of magnitude of available results obtained from different stiffness measurements of ®Ductal FM samples is confirmed. This agreement between analytical and experimental results thus confirms the observations by nanoindentation and XRD investigations (Fig. 9a and b) that the synthesis and processing of UHPC result in a material which is free of weak interface zones.

6. Conclusions

In this paper, the intrinsic properties of the microstructural constituents of a UHPC material cast in real conditions were identified and the nature of fiber–matrix interface was quantitatively examined. The following conclusions can be drawn:

- The C–S–H matrix of UHPC materials is mainly composed of HD C–S–H characterized by intrinsic higher stiffness and hardness values than LD C–S–H that dominates normal *w*/*c* materials.
- A combination of nanoindentation, SEM and XRD provides strong evidence that there is no weak fiber–matrix interface zone in UHPC. We suggest that this is due to the predominant presence of HD C–S–H in UHPC which ensures a uniform composite behavior;
- The use of the measured nano-mechanical properties into a multi-scale upscaling model allows one to link microstructure and constituent properties to macro-mechanical performance of UHPC. Besides confirming the observation of a defect free ITZ, the proposed microstructural model of UHPC, validated here for the elastic properties of UHPC, may serve as well for advanced strength prediction; and more generally as a rational and powerful tool for material-to-structure optimization.

Acknowledgements

Financial support for this study was provided by the OIF Marie Curie FP6 programme. The UHPC bridge deck and material samples were realized within the frame of the French R&D national project MIKTI, sponsored by public research funds “RGCU” , with LCPC, Lafarge, Eiffage and CETE de Lyon. We gratefully acknowledge the NanoMechanical Technology Laboratory in the Department of Materials Science and Engineering at MIT for the nanoindentation testing facility, and Mr. Florent Lespinasse of the Physico-Chimie des Matériaux Division at LCPC, for the SEM and X-ray analysis. Gratefully thanks to Dr. Paul Acker for reviewing the manuscript and Lafarge for making available ® Ductal G2 FM.

References

[1] P. Richard, M. Cheyrezy, Reactive Powder Concretes with high ductility and 200–800 MPa compressive Strength, American Concrete Institute, 1994, pp. 507–518, SP 144–24.
[2] P. Richard, M. Cheyrezy, Composition of reactive powder concretes, Cement and Concrete Research, 25 (7) (1995) 1501–1511.
[3] F. Dutalloir, T. Thibaux, G. Cadoret, G. Birelli, BSI: a new, very high performance concrete, Initial industrial application, The French Technology of Concrete, 13th FIP congress, Amsterdam 1998, pub. AFPC-AFREM, 1998, pp. 25–32.
[4] P. Rossi, High performance multimodal fiber reinforced cement composites (HPMFRCC): the LCPC experience, American Concrete Institute Materials Journal, 94 (6) (1997) 478–483.
[5] B. Graybeal, UHPC in the U.S. highway transportation system, Ultra High Performance Concrete (UHPC), in: Fehling, et al., (Eds.), 2nd International Symposium on Ultra High Performance Concrete, 5–7 March, Kassel, Germany, Kassel, 2008, pp. 11–17.
[6] M. Rebentrost, G. Wight, Experience and applications on ultra-high performance concrete in Asia, in: Fehling, et al., (Eds.), 2nd International Symposium on Ultra High Performance Concrete, 5–7 March, Kassel, Germany, Kassel, 2008, pp. 19–30.
[7] J. Resplendino, Ultra-high performance concrete — recent realizations and research programs on UHPFRC bridges in France, in: Fehling, et al., (Eds.), 2nd International Symposium on Ultra High Performance Concrete, 5–7 March, Kassel, Germany, Kassel, 2008, pp. 31–43.
[8] AFGC-SETRA, Ultra high performance fibre-reinforced concretes, Interim Recommendations, AFGC Publication, France, 2002, p. 152.
[9] Federal Highway Administration, Material property characterization of ultra-high performance concrete, U.S. Department of Transportation, Publication No. FHWA-HRT-06-103, 2006.
[10] M.M. Reda, N.G. Shrive, J.E. Gillott, Microstructural investigation of innovative UHPC, Cement and Concrete Research 29 (1999) 323–329.
[11] M. Cheyrezy, V. Maret, L. Frouin, Microstructural analysis of RPC (Reactive Powder Concrete), Cement and Concrete Research, 25 (7) (1995) 1491–1500.
[12] U. Müller, B. Meng, H.-C. Kühne, J. Nemececk, P. Fontana, Micro texture and mechanical properties of heat and autoclaved Ultra High Performance Concrete (UHPC), in: Fehling, et al., (Eds.), 2nd International Symposium on Ultra High Performance Concrete, 5–7 March, Kassel, Germany, Kassel, 2008, pp. 213–220.
[13] C. Vernet, J. Lukasik, E. Prat, Nanostructure, porosity, perrmeability and diffusivity of UHPC, International Symposium on High-Performance and Reactive Powder Concretes, Sherbrooke, Canada, 2000.
[14] E. Sauzeat, A. Feylessoufi, F. Villiéras, F.J. Yvon, J.M. Cases, P. Richard, Textural analysis of Reactive Powder concretes, in: de Larrard, Lacroix (Eds.), 4th International Symposium on Utilization of HSC/HPC, 29–31 May, Paris, France, 1996, pp. 1359–1365.
[15] G. Chanvillard, S. Rigaud, Complete characterization of tensile properties of Ductal® UHPFRC according to the French recommendations, in: A.E. Naaman, H.W. Reinhardt (Eds.), Proceedings of the 4th International RILEM workshop High Performance Fiber Reinforced Cementitious Composites, 2003, pp. 21–34.
[16] G. Constantinides, F.-J. Ulm, K. Van Vliet, On the use of nanoindetation for cementitious materials, Materials and Structures 36 (257) (2003) 191–196.
[17] G. Constantinides, K.S. Ravi Chandran, F.-J. Ulm, K.J. Van Vliet, Grid indentation analysis of composite microstructure and mechanics: principles and validation, Materials Science and Engineering: A 430 (1–2) (2006) 189–202.
[18] F.-J. Ulm, M. Vandamme, C. Bobko, J.A. Ortega, K. Tai, C. Ortiz, Statistical indentation techniques for hydrated nanocomposites: concrete, bone, and shale, Journal of the American Ceramic Society 90 (9) (2007) 2677–2692.
[19] A.C. Fischer-Cripps, Nanoindentation, Springer Verlag, New-York, 2003.
[20] P. Acker, Micromechanical analysis of creep and shrinkage mechanisms, in: F.-J. Ulm, Z. Bažant, F. Wittman (Eds.), Creep, Shrinkage and Durability Mechanics of Concrete and other Quasi-Brittle Materials, Elsevier, Oxford, UK, 2001, pp. 15–25.
[21] J. Němeček, P. Kabele, Z. Bittnar, Nanoindentation based assessment of micro-mechanical properties of fiber reinforced cementitious composite, in: M. Di Prisco, R. Felicetti, G. Plizzari (Eds.), 6th International Symposium on Fiber Reinforced Concretes BEFIB 2004, 20–22 September, Varenna, Italy, 2004, pp. 401–410.
[22] G. Constantinides, F.-J. Ulm, The effect of two types of C–S–H on the elasticity of cement-based materials: results from nanoindentation and micromechanical modeling, Cement and Concrete Research 34 (1) (2004) 67–80.
[23] G. Constantinides, F.J. Ulm, The nanogranular nature of C–S–H, Journal of Mechanics and Physics of Solids 55 (1) (2007) 64–90.
[24] M.J. DeJong, F.J. Ulm, The nanogranular behavior of C–S–H at elevated temperatures (up to 700C), Cement and Concrete Research 37 (1) (2007) 1–12.
[25] H.M. Jennings, J.J. Thomas, J.S. Gevrenov, G. Constantinides, F.J. Ulm, A multi-technique investigation of the nanoporosity of cement paste, Cement and Concrete Research 37 (2007) 329–336.
[26] Lafarge http://www.ductal-lafarge.fr/wps/portal/Ductal/TechnicalLibrary. (2004).
[27] F. Toutlemonde, J. Resplendino, L. Sorelli, S. Bouteille, S. Brisard, Innovative design of ultra high-performance fiber reinforced concrete ribbed slab, Experimental Validation and Preliminary Detailed Analyses, American Concrete Institute, 2005, pp. 1187–1206, SP-228-76.
[28] F. Toutlemonde, J.C. Renaud, L. Lauvin, A. Simon, M. Behloul, S. Bouteille, J. Resplendino, Experimental validation of a ribbed UHPFRC bridge deck, in: Fehling, et al., (Eds.), 2nd International Symposium on Ultra High Performance Concrete, 5–7 March, Kassel, Germany, Kassel, 2008, pp. 771–778.
[29] M. Miller, C. Bobko, M. Vandamme, F.-J. Ulm, Surface roughness criteria for cement paste nanoindentation, Cement and Concrete Research 38 (4) (2008) 467–476.
[30] L.A. Galin, I.N. Sneddon, Contact problems in theory of elasticity, in: I.N. Sneddon (Ed.), North Carolina State College, 1961, (translated by H. Moss).
[31] I.N. Sneddon, The relation between load and penetration in the axi-symmetric Boussinesq problem for a punch of arbitrary profile, International Journal of Engineering Science 3 (1965) 45–57.

[32] W.C. Oliver, G.M. Pharr, An improved technique for determining hardness and elastic modulus using load and displacement sensing indentation experiments, Journal of Materials Research 7 (6) (1992) 1564–1583.
[33] S. Cariou, F.-J. Ulm, L. Dormieux, Hardness-packing density scaling relations for cohesive-frictional porous materials, Journal of the Mechanics and Physics of Solids, 56 (3) (2008) 924–952.
[34] F.P. Ganneau, F.-J. Ulm, J. Gondzio, E.J. Garboczi, An algorithm for computing the compressive strength of heterogeneous cohesive-frictional materials — application to cement paste, Computers and Geotechnics 34 (4) (2007) 254–266.
[35] B. Gathier, F.J. Ulm, Multiscale strength homogenization — application to shale nanoindentation, MIT CEE Report R08-01, 2008.
[36] G. Constantinides, F.-J. Ulm, The elastic properties of calcium leached cement pastes and mortars: a multi-scale investigation, MIT CEE Report R02-01, 2006.
[37] G. Constantinides, E.C.C. Silva, G.S. Blackman, K.J. van Vliet, Dealing with imperfection: quantifying potential length scale artefacts from nominally spherical indenter probes, Nanotechnology 18 (30) (2007) 305503.
[38] K. Velez, S. Maximilien, D. Damidot, G. Fantozzi, F. Sorrentino, Determination by nanoindentation of elastic modulus and hardness of pure constituents of Portland cement clinker, Cement and Concrete Research 31 (4) (2001) 555–561.
[39] P. Mondal, P.S. Shah, L. Marks, A reliable technique to determine local mechanical properties at nanoscale for cementitious material, Cement and Concrete Research 37 (2007) 1440–1444.
[40] P. Mondal, S.P. Shah, L.D. Marks, Nanoscale characterization of cementitious materials, ACI Materials Journal 105 (2) (2008) 174–180 Farmington Hills: Mar/Apr 2008.
[41] S. Mindess, A. Bentur, Fibre Reinforced Cementitious Composites, Elsevier Applied Science, London and New York, 1990.
[42] A. Zaoui, Continuum micromechanics: survey, Journal of Engineering Mechanics, ASCE 128 (8) (2002) 808–816.
[43] L. Dormieux, D. Kondo, F.J. Ulm, Microporomechanics, John Wiley and Sons, Ltd, West Sussex, England, 2006.
[44] T. Mori, K. Tanaka, Average stress in matrix and average elastic energy of materials with misfitting inclusions, Acta Metallica 21 (5) (1973) 571–574.
[45] J.D. Eshelby, The Determination of the Elastic Field of an Ellipsoidal Inclusion and Related Problems, vol. A241, Proc. Royal Society, London, 1957, pp. 376–396.
[46] Astm C457, Standard test method for microscopical determination of parameters of the air-void system in hardened concrete, American Society for Testing and Materials Standard Practice C457, Philadelphia, PA, 1998.
[47] ASTM C469, Standard test method for static modulus of elasticity and Poisson's ratio of concrete, Compression, American Society for Testing and Materials Standard Practice C469, Philadelphia, PA, 1994.